

● Original Contribution

ENHANCEMENT AND PASSIVE ACOUSTIC MAPPING OF CAVITATION FROM FLUORESCENTLY TAGGED MAGNETIC RESONANCE-VISIBLE MAGNETIC MICROBUBBLES *IN VIVO*

CALUM CRAKE,* JOSHUA OWEN,* SEAN SMART,[†] CHRISTIAN COVIELLO,* CONSTANTIN-C. COUSSIOS,*
 ROBERT CARLISLE,* and ELEANOR STRIDE*

*Institute of Biomedical Engineering, Department of Engineering Science, University of Oxford, Oxford, UK; and [†]Gray
 Institute for Radiation Oncology and Biology, Radiobiology Research Institute, Churchill Hospital, Oxford, UK

(Received 9 May 2016; revised 24 July 2016; in final form 1 August 2016)

Abstract—Previous work has indicated the potential of magnetically functionalized microbubbles to localize and enhance cavitation activity under focused ultrasound exposure *in vitro*. The aim of this study was to investigate magnetic targeting of microbubbles for promotion of cavitation *in vivo*. Fluorescently labelled magnetic microbubbles were administered intravenously in a murine xenograft model. Cavitation was induced using a 0.5-MHz focused ultrasound transducer at peak negative focal pressures of 1.2–2.0 MPa and monitored in real-time using B-mode imaging and passive acoustic mapping. Magnetic targeting was found to increase the amplitude of the cavitation signal by approximately 50% compared with untargeted bubbles. Post-exposure magnetic resonance imaging indicated deposition of magnetic nanoparticles in tumours. Magnetic targeting was similarly associated with increased fluorescence intensity in the tumours after the experiments. These results suggest that magnetic targeting could potentially be used to improve delivery of cavitation-mediated therapy and that passive acoustic mapping could be used for real-time monitoring of this process. (E-mail: eleanor.stride@eng.ox.ac.uk) © 2016 The Authors. Published by Elsevier Inc. on behalf of World Federation for Ultrasound in Medicine & Biology. This is an open access article under the CC BY license (<http://creativecommons.org/licenses/by/4.0/>).

Key Words: Ultrasound, Magnetic microbubbles, Passive acoustic mapping, Cavitation, Drug delivery, Fluorescence, Magnetic resonance imaging.

INTRODUCTION

Ultrasound (US) has previously been found to have therapeutic benefits for a diverse range of applications including physiotherapy (Patrick 1966), cancer treatment (Kremkau 1979), non-invasive surgery (ter Haar 1999) and enhancement of the delivery of various agents such as genes (Newman et al. 2001), chemotherapeutics (Unger et al. 1998) and oncolytic viruses (Carlisle et al. 2013). At lower amplitudes, ultrasound may be used to temporarily disrupt the blood–brain barrier, facilitating the delivery of drugs to the central nervous system (Hynynen et al. 2006), whereas higher-intensity regimes

may be used to deliver drugs to tumours (Lafon et al. 2012) or to facilitate non-invasive surgery by enabling instigation of tissue fractionation (Roberts et al. 2006) or ablation (Illing et al. 2005) from outside of the body.

Acoustic cavitation has been found to play a key role in the bio-effects of ultrasound (Coussios and Roy 2008) and may be significantly enhanced by the addition of exogenous cavitation nuclei such as acoustically active microbubbles (Greenleaf et al. 1998; Miller and Thomas 1995). Microbubbles are commonly used as ultrasound contrast agents for imaging (Ferrara et al. 2007) and may also be formulated to provide additional functionality for diagnosis and therapy. For diagnostic purposes, the incorporation of iron oxide nanoparticles into the microbubble formulation can enable them to provide contrast enhancement in both ultrasound and magnetic resonance imaging (MRI) (Liu et al. 2011; Yang et al. 2009). Alternatively, fluorescent dyes can be used to render microbubbles fluorescent (Lum et al. 2006; Patil et al. 2011), allowing tracking of the distribution

Address correspondence to: Eleanor Stride, Institute of Biomedical Engineering, University of Oxford, Old Road Campus Research Building, Oxford OX3 7DQ, UK. E-mail: eleanor.stride@eng.ox.ac.uk

Data repository: The data from which the results presented in this paper are derived may be found at <http://dx.doi.org/10.5287/bodleian:wrw8Xrp24>.

of microbubble components using fluorescence imaging techniques. Both MRI contrast enhancement and fluorescence labelling were employed in the study described here.

To maximise their impact, microbubbles may also be formulated to incorporate a therapeutic payload (Hua *et al.* 1993; Lentacker *et al.* 2009), which will then be released upon ultrasound exposure at the treatment site. This effect may be further enhanced if the microbubbles are targeted to their intended site of action using strategies such as incorporation of antibodies into the microbubble shell, thereby allowing specific binding to receptors on target cells (Villanueva *et al.* 1998). However, the efficacy of such biological targeting methods is strongly influenced by flow conditions (Takalkar *et al.* 2004) and requires the microbubbles to come within very short distances (on the order of nanometres) of their intended site (Ham *et al.* 2009). Targeting on greater length scales may be achieved by applying an external stimulus, such as by exploiting acoustic radiation forces (Dayton *et al.* 1999). Alternatively, incorporation of magnetic material such as iron oxide nanoparticles into the microbubble formulation can enable localisation using a magnetic field (Plank *et al.* 2005). Such methods were used in this study to facilitate magnetic targeting of microbubbles.

In previous work, magnetic microbubbles (MMBs) were reported to enhance ultrasound-mediated gene delivery both *in vitro* (Mannell *et al.* 2012; Stride *et al.* 2009; Vlaskou *et al.* 2010b) and *in vivo* (Mulvana *et al.* 2010; Vlaskou *et al.* 2010a). However, the underlying mechanisms were not explored in detail; in particular, acoustic monitoring in previous studies was limited. In a recent study by the authors, it was found that magnetic localisation of microbubbles was associated with increased cavitation activity *in vitro*, assessed using passive acoustic mapping (PAM) of their acoustic emissions (Crake *et al.* 2015). The purpose of the present study was to establish whether similar effects could be observed in the cavitation behaviour of magnetic microbubbles *in vivo* and to assess the distribution of microbubble components using fluorescence methods and MRI.

METHODS

Magnetic microbubble production

1,2-Distearoyl-*sn*-glycero-3-phosphocholine dissolved in chloroform (DSPC, 25 mg/mL) was purchased from Avanti Polar Lipids (Alabaster, AL, USA). Polyoxyethylene-40-stearate (PEG), chloroform, glycerol and propylene glycol were purchased from Sigma Aldrich (Gillingham, Dorset, UK). 1,1'-Dioctadecyl-3,3',3'-tetramethylindocarbocyanine perchlorate (DiI) stain and phosphate-buffered saline (PBS) were purchased from Life Technologies (Paisley, UK). FluidMAG-Lipid

(25 mg/mL 50-nm spherical phosphatidylcholine-coated magnetite particles in sterile water) was purchased from Chemicell (Berlin, Germany). Sulphur hexafluoride (SF₆) was purchased from BOC (Guildford, UK).

PEG was dissolved in chloroform (10 mg/mL) using a bath sonicator. DiI was dissolved in chloroform (2.5 mg/mL). DSPC and PEG solutions were mixed in a 9:1 molar ratio (61 μ L of 25 mg/mL DSPC solution, 44 μ L of 10 mg/mL PEG solution) in a glass vial. Glass precision syringes (Hamilton Microliter; Sigma-Aldrich, Gillingham, Dorset, UK) were used to measure solutions for chloroform resistance. For fluorescence labelling of the MMBs, 20 μ L of DiI solution was added to the mixture, and the vial was left on a hot plate at 50°C for 12 h in a fume hood to allow the chloroform to evaporate. The resulting lipid film was resuspended in 1.5 mL of a solution consisting of 80% PBS, 10% glycerol and 10% propylene glycol on a hot plate at 70°C with constant stirring for 20 min. The solution was then sonicated for 60 s to disperse the lipids using an ultrasonic cell disruptor (tip fully immersed, power setting 2; Model XL 2000, 3-mm probe diameter, 22.5 kHz, Misonix, Farmingdale, NY, USA). Fifteen microliters of FluidMAG-Lipid solution was added to the vial, and sonication was repeated for 10 s. To produce microbubbles, the probe tip was moved to the air-liquid interface, and sonication was repeated for 10 s (power setting 15) while SF₆ was continuously delivered from the gas cylinder to the vial *via* a tube held close to the vial opening. After sonication, the vial was immediately sealed using a pierceable stopper and stored on ice until used. Experiments commenced within 1 h of sonication.

In vitro microbubble characterisation

Sizing. Microbubble size distribution and concentration were determined *via* optical microscopy (Model Eclipse Ti-E, Nikon Instruments, UK) using a 20 \times objective lens (Model Plan Fluor, Nikon Instruments, UK). A 20- μ L sample of the microbubble suspension was pipetted onto a slide, and 30 images were taken in different locations. Particle size distribution and concentration were then determined using purpose-written software (Sennoga *et al.* 2010) in MATLAB (The MathWorks, Natick, MA, USA).

Fluorescence labelling. To confirm that the lipophilic dye DiI could fluorescently label the microbubbles, samples were examined using a fluorescence microscope (Eclipse Ti-E, Nikon Instruments, UK) fitted with a 20 \times objective (Plan Fluor, Nikon Instruments, Kingston-upon-Thames, UK), mercury arc light source and TRITC filter cube. Brightfield and fluorescence images were taken of the same fields of view.

Magnetic response. To confirm that microbubbles were magnetically responsive, samples were pipetted onto a slide without a coverslip (the buoyancy of the microbubbles against the coverslip was found to impede motion when a coverslip was used) and examined using a $4\times$ objective (Plan Fluor). The field of view was positioned toward one edge of the sample while a 1.5-T permanent magnet (N52 grade NdFeB, $10 \times 10 \times 25$ mm; NeoTegg, Berlin, Germany) was held above the same side of the slide. Images of the same field of view were taken in both brightfield and fluorescence modes.

Acoustic response. To confirm that the microbubbles were responsive under B-mode and focused ultrasound excitation, a simplified version of the experimental setup for the *in vivo* work was used (see below). Ten percent by volume microbubble suspension or water was placed in a cylindrical sample holder (internal dimensions: 20-mm diameter \times 20-mm depth) with acoustically transparent Mylar windows on both sides to allow for ultrasound propagation. Microbubbles were delivered using the same-model 29-gauge needle and insulin syringe as used for the *in vivo* experiments. The central volume of the sample chamber was aligned with the focus of the focused ultrasound (FUS) transducer in a water tank. B-Mode images were recorded with the FUS transducer disabled for 10 s over a range of transmit amplitudes (transmit voltage: 1.6–11.3 V). B-Mode (6.5-V transmit voltage) and passively recorded radiofrequency data for PAM were then acquired for 30 s with focused ultrasound excitation over a range of amplitudes (0–2.0 MPa peak negative focal pressure, 100 cycles per burst).

Experimental setup for *in vivo* work

An overview of the experimental setup is given in Figure 1. Ultrasound was generated using a 500-kHz spherically focused single-element FUS transducer (Model H-107 B-10, Sonic Concepts, Bothell, WA, USA) with an outer diameter of 64 mm and focal length of 63 mm and featuring a 45×18 -mm rectangular cutout through which an imaging linear array probe (Model L11-4 v, Verasonics, Kirkland, WA, USA) with 128 elements, 38-mm aperture and 4- to 11-MHz bandwidth was aligned such that the focus of the FUS transducer was within the imaging plane. Driving waveforms were generated using a function generator (Model 33250 A, Agilent, Wokingham, Berkshire, UK) synchronised to the ultrasound research platform (Model Vantage 256, Verasonics) using a trigger output signal. The driving signal was applied to the FUS transducer via a 55-dB power amplifier (Model 1040 L, Electronics and Innovation, Rochester, NY, USA) and impedance matching network supplied by the transducer manufacturer. The ultrasound

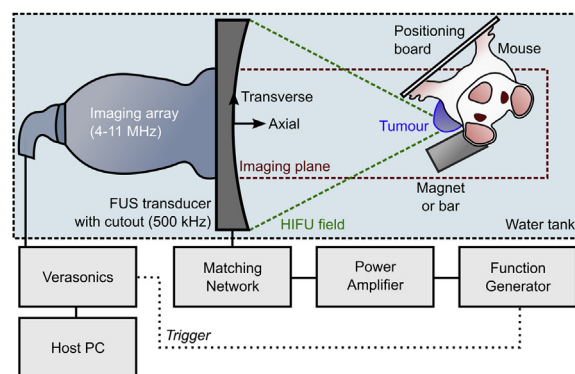


Fig. 1. Overview of the setup for *in vivo* experiments (plan view, not to scale). Tumours were aligned with the focus of a 500-kHz focused ultrasound (FUS) transducer with a rectangular cut-out for a 4- to 11-MHz imaging array. B-Mode imaging was interspersed with passive acoustic recording of the emissions from cavitation during FUS transducer pulses. Transverse and axial directions are defined relative to the centre of the front face of the imaging array. Exposures were performed in the presence of a magnet or non-magnetic bar.

research platform was connected to a host desktop PC to configure the imaging sequence, save data and provide real-time display during experiments.

The FUS transducer and imaging array assembly were mounted using a three-axis positioning stage in a $40 \times 40 \times 17$ -cm acrylic tank filled with filtered, degassed, de-ionised water that was heated to 37°C using an immersion heater. Water quality was maintained during experiments by continuous flow through a loop consisting of a centrifugal pump, de-ionisation column, $10\text{-}\mu\text{m}$ filter and vacuum degassing membrane. That the degassing process had been successful was tested by activating the FUS transducer and observing the acoustic emissions using the linear array to confirm absence of cavitation from the water. Before commencing experiments, the focus of the FUS transducer was located using a $75\text{-}\mu\text{m}$ needle hydrophone (Precision Acoustics, Dorchester, UK). The location of the hydrophone tip observed under B-mode imaging was recorded for display as an overlay on the B-mode image after the hydrophone was removed, and used to position tumours at the focus during experiments. A single rectangular permanent magnet (N52 grade NdFeB, $10 \times 10 \times 25$ mm, NeoTegg, Berlin, Germany) with transversal magnetisation 1.5 T or non-magnetic stainless-steel bar of the same dimensions was held in a clamp attached to a three-axis positioning stage and placed close to the focus of the FUS transducer. The magnet or bar was placed at an angle with respect to the ultrasound array to reduce direct reflection of the ultrasound and creation of standing waves. A acrylic board attached to a three-axis positioning stage was used to secure mice and align tumours with the focus of the FUS transducer under B-

mode guidance. A nose piece attached to the positioning board was used for delivery of anaesthetic during the experiments.

Ultrasound research platform configuration

The ultrasound research platform was configured to provide B-mode harmonic imaging (4.5-MHz transmit, 9-MHz receive, 48 pulse-inversion pairs per frame, 48 active elements per transmit, 10-cm imaging depth) interleaved with passive recording of the acoustic emissions from cavitation (array transmit disabled; receive on 128 channels, 35-MHz sample rate, 250- μ s recording length) at an overall frame rate of 0.5 Hz. A trigger output signal was sent at the beginning of passive recording to the function generator to initiate focused ultrasound excitation at the same pulse repetition frequency. Data were transferred during experiments from the research platform over a PCI-express bus to a host PC running MATLAB for real-time display.

B-Mode image reconstruction was accomplished using compounding of the 96 received signals per frame with built-in routines supplied by the system manufacturer. Passively recorded data were processed using a 1-MHz high-pass digital filter (to attenuate the 0.5-MHz FUS drive signal) and implementation of the time exposure acoustics algorithm as previously described (Gyöngy and Coussios 2010). Passive maps of 20×24 pixels were produced over a 10-mm (transverse) \times 20-mm (axial) region centred on the focus of the FUS transducer. B-Mode images, passive acoustic maps and radio-frequency (RF) data for selected elements were displayed in real time during experiments. Images and raw RF channel data were saved to disk for analysis after the experiments.

Animal model

Animal experiments were conducted in accordance with UK Home Office guidelines. Balb/c mice (female, 6–8 wk old, mass: 20.0 ± 1.3 g; Harlan, UK) were injected subcutaneously with CT26 cells (2×10^5 per mouse; ATCC; LGC Standards, Teddington, UK) and allowed to form tumours approximately 100–200 mm³ in size before commencing experiments.

In vivo experimental protocol

Tumours were depilated using depilatory cream (Veet, Reckitt Benckiser), thoroughly rinsed with water to prevent trapping of air and outlined with a marker pen to aid in visual alignment. Mice were anaesthetised using 5% isoflurane, attached to the positioning board with tape and maintained under anaesthesia using a nose piece connected to the positioning board delivering 2% isoflurane. Tail veins were cannulated using a 29-gauge needle attached to an insulin syringe *via* a short

length of 0.3-mm-inner diameter plastic tubing primed with PBS, such that the syringe could remain outside of the water tank. Mice were placed vertically in the tank (head and ears above water surface), and tumours were aligned with the previously identified FUS transducer focus under B-mode guidance. The magnet or non-magnetic bar was positioned close to the tumour at an angle with respect to the axis of propagation to minimise disruption of the ultrasound field. Samples of magnetic microbubbles (150 μ L) were drawn through the pierceable lid of the vial into an insulin syringe shortly before the start of each experiment. Each mouse was treated three times. For each treatment 50 μ L of the microbubble suspension was injected *via* the tail vein cannula. Between treatments the FUS transducer and imaging array assembly were moved by 3 mm in the vertical direction such that the focus was moved within the tumour.

To begin each experiment, saving of B-mode and passive data and focused ultrasound excitation where applicable were simultaneously initiated. After 1 min, the first 50- μ L dose of microbubbles was injected. After a further 2 min, the transducer assembly was moved 3 mm in the vertical direction. The procedure was then repeated twice, giving three injections per mouse in a total treatment time of 9 min. The ultrasound platform was then paused to stop treatment, the mice were promptly removed from the tank, the cannulae were removed and the mice were allowed to recover in a warm box. At 15 min from the first injection, mice were euthanized by cervical dislocation, and 20 μ L of blood drawn from the tail vein, which was made up to 200 μ L with PBS and centrifuged for 2 min at 3000 rpm. Plasma and insoluble components were frozen separately at -20°C . Tumours were harvested and frozen at -20°C .

For analysis of the distribution of microbubble components using fluorescence measurements, the liver, spleen, lungs, kidneys, tumour and blood samples were extracted from six mice after euthanasia 15 min after treatment with MMBs with or without a magnet and compared with samples to which known dilutions of MMBs were added. To investigate clearance kinetics blood and liver samples were taken from six additional mice at 10 min from treatment. To establish the *in vivo* cavitation threshold for magnetic microbubbles (and define the ultrasound conditions for the main part of the study), three mice were treated with MMBs and focused ultrasound excitation (frequency: 500 kHz, 100 cycles per burst, 0.5-Hz pulse repetition frequency) at peak negative focal pressures of 1.2, 1.6 and 2.0 MPa respectively. Next, to evaluate the effects of magnetic targeting on the cavitation behaviour of MMBs, eight mice were treated with focused ultrasound (1.6-MPa peak negative focal pressure) with either MMBs, MMBs + magnet, SonoVue + magnet or 24-h-old (depleted) MMBs. A

non-magnetic metal bar was used for experiments not using the magnet. The commercial contrast agent SonoVue was used as a non-magnetic control in the presence of the magnet and as a reference for comparison of the cavitation behaviour of MMBs. A 24-h-old sample of MMBs was used to compare the response and distribution of a sample with similar chemical composition but depleted bubble concentration and hence lower acoustic response. Finally, to evaluate the effects of magnetic targeting on cavitation-enhanced delivery of dye and magnetic particles, six mice were treated with either MMBs, MMBs + magnet, SonoVue + magnet, 24-h-old (depleted) MMBs or saline. Two mice (treated with MMBs + magnet or saline) were frozen intact after euthanasia for whole-body MRI. Tumours were extracted from the remaining mice for estimation of microbubble content using fluorescence measurements.

Biological sample processing

Plasma/PBS samples were defrosted, stored on ice and protected from light. The fluorescence of 100- μ L samples was measured in a black 96-well plate using a plate reader (excitation: 544 nm, emission: 590 nm, gain: 2000; FLUOstar Omega, BMG LABTECH, Aylesbury, UK) and compared with a standard curve prepared from known quantities of microbubbles in plasma. Tissue samples were defrosted, weighed using a balance with 0.1 mg precision (Explorer Pro, OHAUS, Nänikon, Switzerland) and homogenised in PBS using a rotary homogenizer (Model T10 basic, IKA, Staufen, Germany) to a concentration of 200 mg tissue per mL buffer. Samples were stored on ice and protected from light during the procedure. The fluorescence of 100- μ L samples was measured and compared with that of standard samples containing known quantities of microbubbles homogenised in tissue.

Magnetic resonance imaging

MRI was performed at 4.7 T (VNMRS, Varian, Palo Alto, CA, USA) using a whole-mouse-body quadrature birdcage transmit–receive coil (Rapid Biomedical, Rimpar, Germany). Progressively T2*-weighted imaging was performed using a 3-D multiple gradient echo scan with echo times, TE = 3.65, 9.78, 15.91 and 22.04 ms, repetition time, TR = 50 ms and flip angle = 30°, at an isotropic resolution of $\sim 211 \mu\text{m}$ covering a field of view of $108 \times 27 \times 27 \text{ mm}$ in a scan time of 14 min. Shimming, frequency offset adjustment and RF pulse calibration were performed for each sample, and scans on different samples were operated with the same receiver gain settings. Images were exported to TIFF files ($512 \times 128 \times 128 \text{ pixels} \times 4 \text{ echo times}$; 32 bits per pixel, 128 MB per file) for analysis in ImageJ (US National Institutes of Health, Bethesda, MD, USA). Slices

revealing the liver and tumour in each mouse were selected, and the borders of these regions outlined manually using the freehand selection tool and saved as regions of interest using the ROI manager feature. The mean and standard deviation of image intensity in each ROI were measured at each of the four echo times. To account for intensity inhomogeneity (Vovk et al. 2007), the results for liver and tumour were normalised using the mean image intensities in nearby areas of muscle at the same echo times.

PAM post-processing

After the experiments the passively recorded data were reprocessed over a larger grid ($40 \times 36 \text{ pixels}$, $20 \times 30 \text{ mm}$) using a robust beamforming algorithm (Coviello et al. 2015) to improve the resolution of mapping and ensure all cavitation activity was captured in the region of interest. The maximum value in each pixel over the duration of the experiments (indicating maximum cavitation power) was overlaid in the corresponding location on the B-mode images to produce representative spatial maps of cavitation activity for each experiment. The maximum cavitation power was also extracted from each frame of data to determine the evolution of cavitation behaviour over time (in particular, the effects of microbubble injection and destruction). To produce spectra of the emissions during pressure ramp experiments, the passively recorded data from the 128 channels in each frame were beamformed to obtain a trace corresponding to the focal point and then subjected to a Fourier transform (MATLAB function *fft*). The spectra at each time point were averaged over the duration of the experiments and plotted over the range 0–10 MHz (toward the upper end of the frequency response of the ultrasound array, and corresponding to 20 harmonics of the focused ultrasound excitation frequency).

RESULTS AND DISCUSSION

In vitro MMB characterisation

Sizing. The results of microbubble sizing measurements are illustrated in Figure 2a. The measured microbubble concentration of $1.8 \times 10^8 \text{ microbubbles/mL}$ and mean diameter of $3.1 \mu\text{m}$ were both similar to those of commercial clinically approved contrast agents (e.g., $1\text{--}5 \times 10^8 \text{ microbubbles/mL}$ and $2.5\text{--}\mu\text{m}$ mean diameter for SonoVue) (Schneider 1999).

Fluorescence labelling. Figure 2b and c are bright-field and fluorescence images of the same field of view of a sample of magnetic microbubbles. Comparison of the two images confirms that the lipophilic dye is attracted to the lipid-based microbubble shells, which are

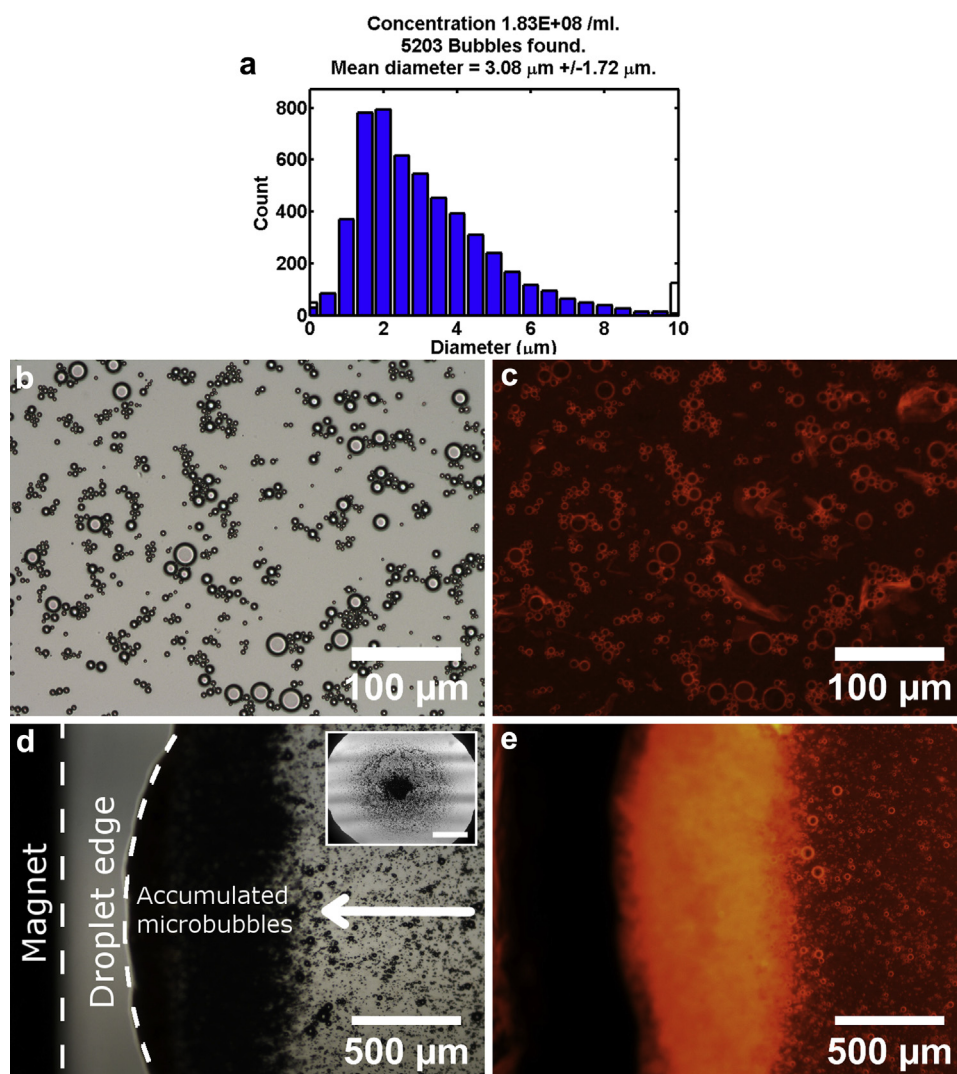


Fig. 2. *In vitro* magnetic microbubble (MMB) characterisation. (a) Size distribution plot obtained from 30 images of magnetic microbubbles using the image processing software. (b, c) Microscope images of magnetic microbubbles ($20\times$ objective): (b) brightfield (33-ms exposure, $1\times$ gain) and (c) fluorescence (TRITC filter, 500-ms exposure, $1\times$ gain) images of the same field of view. (d) Brightfield and (e) fluorescence (TRITC filter) microscope images of magnetic microbubbles ($4\times$ objective) under influence of a magnet. Microbubbles were pipetted into a droplet, and the field of view was positioned toward the left edge of the droplet. A 1.5-T permanent magnet was held above the left side of the slide and is visible as the dark region to the left of the brightfield image. Microbubbles were observed to move toward the magnet and gather on the side of the droplet closest to the magnet under both brightfield and fluorescence imaging. Arrow in (d) indicates direction of microbubble motion. Inset in (d) depicts the initial distribution of microbubbles in the centre of droplet before application of magnetic field taken at $1\times$ magnification (bar = $2000\text{ }\mu\text{m}$).

clearly visible against the background in the fluorescence image.

Magnetic response. Microscope images revealing magnetic microbubbles under the influence of a magnetic field are provided in Figure 2d and e. Notably, the use of a coverslip on the microscope slide was found to impede microbubble motion, in contrast to previous work with magnetic microbubbles containing an oil-based ferrofluid (Crake *et al.* 2015). It

was hypothesised that this could be due to the lack of an oil layer in the new formulation, resulting in more buoyant microbubbles. For this reason, the microbubble sample was pipetted onto a slide and left in a droplet, the microscope field of view being positioned toward one edge of the droplet. When a 1.5-T permanent magnet was brought close to the microscope slide, microbubbles were observed to move toward it and gather on this side of the droplet (Fig. 2d). Observation of the same field of view under

fluorescence (TRITC filter) revealed strong emissions in the same region (Fig. 2e), which suggests successful co-localisation of magnetic particles and fluorescent dye within the microbubbles.

Acoustic response. In Figure 3 are B-mode and PAM images from *in vitro* measurements of the magnetic microbubbles in a sample holder. The outline of the sample holder and reflections from the front and rear Mylar walls are clearly visible in the B-mode image for the sample holder containing water (Fig. 3a), with negligible echo within the chamber. When 10% MMBs were added (Fig. 3b), a strong increase in image contrast was observed within the sample chamber.

When the 500-kHz focused transducer was activated and the PAM data were processed (Fig. 3c, d) only very low amplitude signals (corresponding to the electrical noise floor of the system) were observed using water (Fig. 3c), with a >1000 -fold increase in peak power when MMBs were added (Fig. 3d) (peak power: 0.34 W vs. 0.0002 W). The location of the peak in power in the maps correlates well with the previously measured focal point of the FUS transducer, which was positioned in the centre of the sample chamber.

Distribution of magnetic microbubbles *in vivo*

The distribution of magnetic microbubbles in mice based on fluorescence measurements is illustrated in Figure 4a. Six mice were injected with magnetic microbubbles without therapeutic ultrasound exposure with either a magnet or a non-magnetic bar positioned close to the tumour. Fluorescence readings were converted to microbubble concentration by use of a standard curve composed of known microbubble quantities spiked into blank samples. Concentration measurements for blood were scaled to obtain total circulating volume based on the weight of each mouse and assuming 72 mL blood/kg mouse weight (Diehl et al. 2001). Organ measurements were scaled to total volume in each organ based on the measured mass of each organ before homogenisation.

Fluorescence readings indicate that a DiI concentration corresponding to an average of 16% ($\pm 2\%$) of the injected dose was measured in the blood after 15 min, with no significant difference between control and magnet runs ($p = 0.10$). Linear extrapolation ($R^2 = 0.999$) of the mean result at 10 min (assuming 100% initial value) (Fig. 4b) suggests a clearance time of around 18 min. This result suggests that

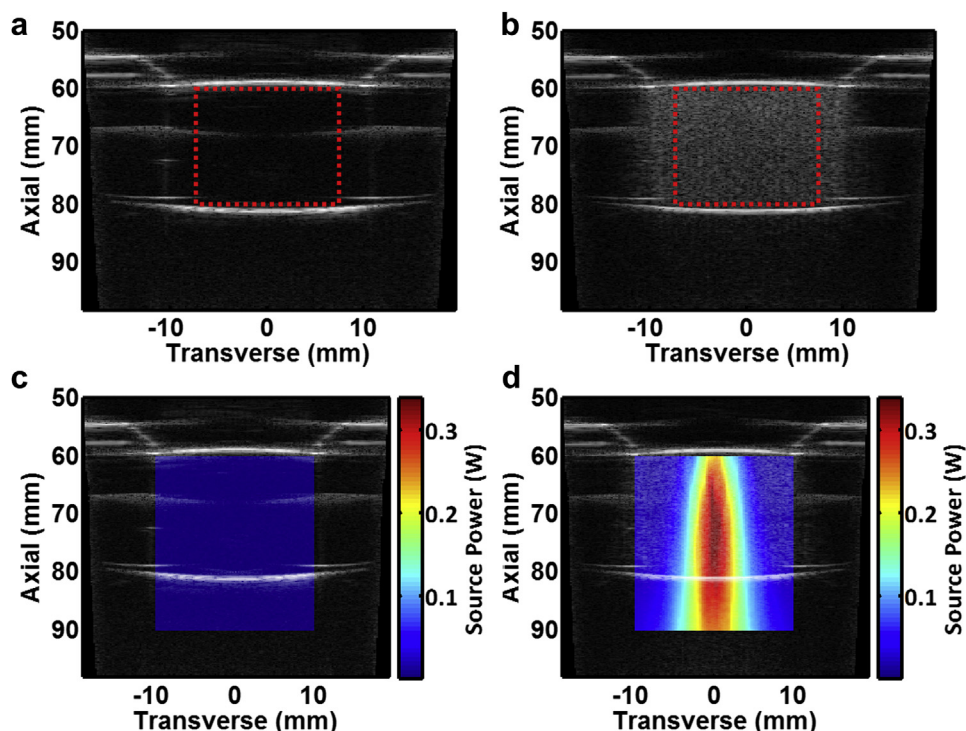


Fig. 3. (a, b) *In vitro* acoustic testing of magnetic microbubbles under B-mode imaging. A region of interest (ROI) within the sample holder is represented by the red dotted box. B-Mode images for the sample holder containing (a) water and (b) 10% by volume magnetic microbubbles (MMBs). (c, d) *In vitro* acoustic testing of magnetic microbubbles under focused ultrasound excitation. B-Mode images with passive acoustic mapping (PAM) overlay showing maps of source power for (c) water and (d) 10% by volume MMBs.

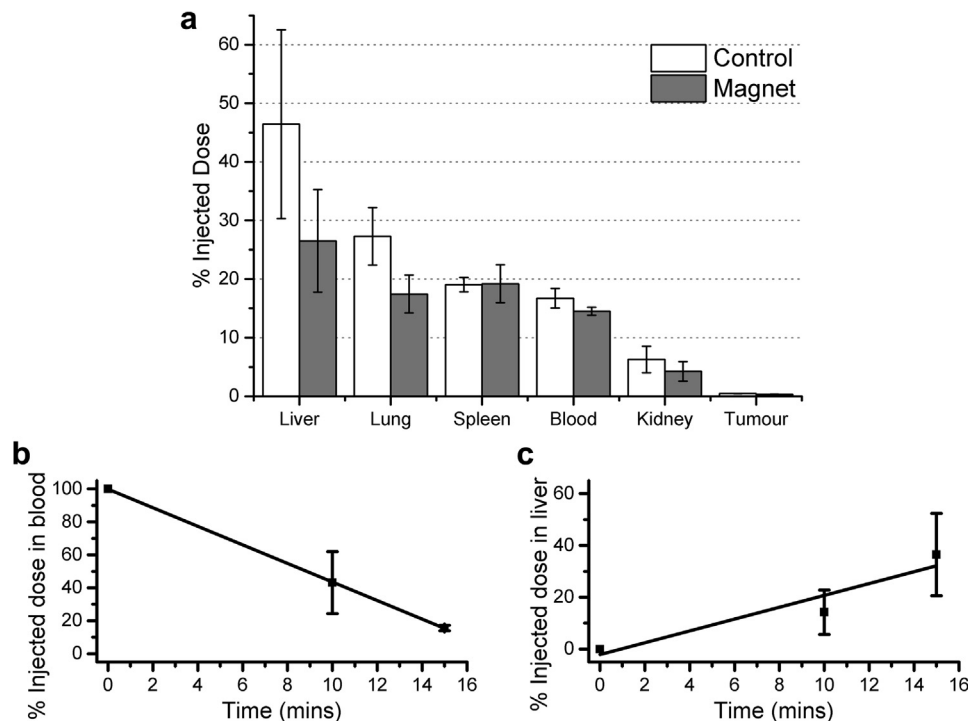


Fig. 4. Percentage of injected dose in blood and organs of mice following experiments. (a) Distribution in blood and organs at 15 min. Mice were injected with microbubbles while either a magnet ($n = 3$) or non-magnetic bar ($n = 3$) was positioned close to the tumour. (b, c) Comparison of percentage doses in blood and liver at 10 and 15 min reveals approximately linear behaviour (R^2 values: 0.999 and 0.903, respectively). Means \pm standard deviations of all six mice is shown. Initial doses of 100% and 0% were assumed for blood and liver, respectively.

microbubble components were still present after several minutes, which is a practical time scale for drug delivery applications. Of the major organs, the highest uptake of MMBs was seen in the liver (mean $36 \pm 16\%$ of injected dose). Again, the mean result at 10 min exhibits approximately linear behaviour ($R^2 = 0.903$, assuming zero initial value) (Fig. 4c). This is in line with previous work using magnetic nanodroplets (Cheng *et al.* 2013) and microbubbles (Barrefelt *et al.* 2013) that revealed high uptake of similar particles in the liver, which is believed to involve capture by macrophages (in particular Kupffer cells) in the reticuloendothelial system. Strong uptake in the liver was also suggested by contrast from the iron content of the bubbles under MRI (see below).

The dose found in the lungs (mean: $22 \pm 7\%$) was encouragingly low (*i.e.*, of a magnitude similar to that remaining in the blood) as microbubbles were delivered *via* tail vein injection and so would pass the lungs before reaching other organs *via* the systemic circulation. The lungs have previously been reported to trap microbubbles, particularly those of larger size ($>20 \mu\text{m}$) (Butler and Hills 1979). A significant reduction ($p = 0.04$) was observed between control and magnet-treated mice, implying that magnetic targeting may have reduced the

proportion of microbubbles trapped in the lungs, perhaps by retaining some of the larger microbubbles (which would be both most likely to be trapped in the lungs and also to contain the greatest quantity of magnetic material). Previous *in vivo* histologic work using similar microbubbles indicated that the concentration in the lungs is initially at its peak value before falling (whereas that in clearance organs such as the liver and spleen rises over time) (Barrefelt *et al.* 2013).

The dose found in the spleen in these experiments was lower than that of the liver (mean $19\% \pm 2\%$ of injected dose). This is in agreement with previous work that revealed under histologic analysis that the quantity of microbubbles in the spleen was initially low, reaching a peak value after 24 h and declining thereafter (Barrefelt *et al.* 2013). Only a small proportion of the injected dose was found in the kidney (mean: $5 \pm 2\%$), again in agreement with previous studies (Barrefelt *et al.* 2013; Cheng *et al.* 2013). Within the tumours, only a small (but detectable) average $0.39 \pm 0.08\%$ of the injected dose was found. Therapeutic excitation was not used in this set of experiments so this measurement represents the background volume of microbubbles or unbound dye retained in tumour vasculature. Overall for the six mice it was possible to recover on average $99 \pm 22\%$ of the

injected dose from samples taken. Owing largely to reductions in the values for liver and lungs, the total recovery was significantly lower (mean: 83% vs. 117%, $p = 0.03$) in magnet-treated mice. The remaining portion in magnet-treated mice may be accounted for by tissue that was not sampled in these experiments such as the skin surrounding the tumour.

In vivo cavitation threshold of magnetic microbubbles

B-Mode and PAM data for the *in vivo* pressure ramp experiments are illustrated in Figure 5. At 1.2 MPa peak negative focal pressure (Fig. 5a), some cavitation was observed within the tumour (peak power: 29.2 mW).

Over the duration of the experiment (Fig. 5d, blue line) cavitation was sporadic, with minor peaks visible at the injection times (21.5, 10.8 and 1.5 mW at 1, 4 and 7 min respectively). Spectra of the received signal (Fig. 5e, blue line) indicated the 500-kHz excitation frequency and harmonics at 1 and 1.5 MHz only.

At 1.6 MPa peak negative focal pressure (Fig. 5b), the amplitude of cavitation emissions was increased by a factor of 5 (peak power: 152.9 mW), and clearly distinct peaks were visible at the injection times (peak values 152.9, 83.0 and 48.7 mW at 1, 4 and 7 min) (Fig. 5d, green line). Spectra of the received signal (Fig. 5e, green line) now depicted a typical microbubble response (Leighton

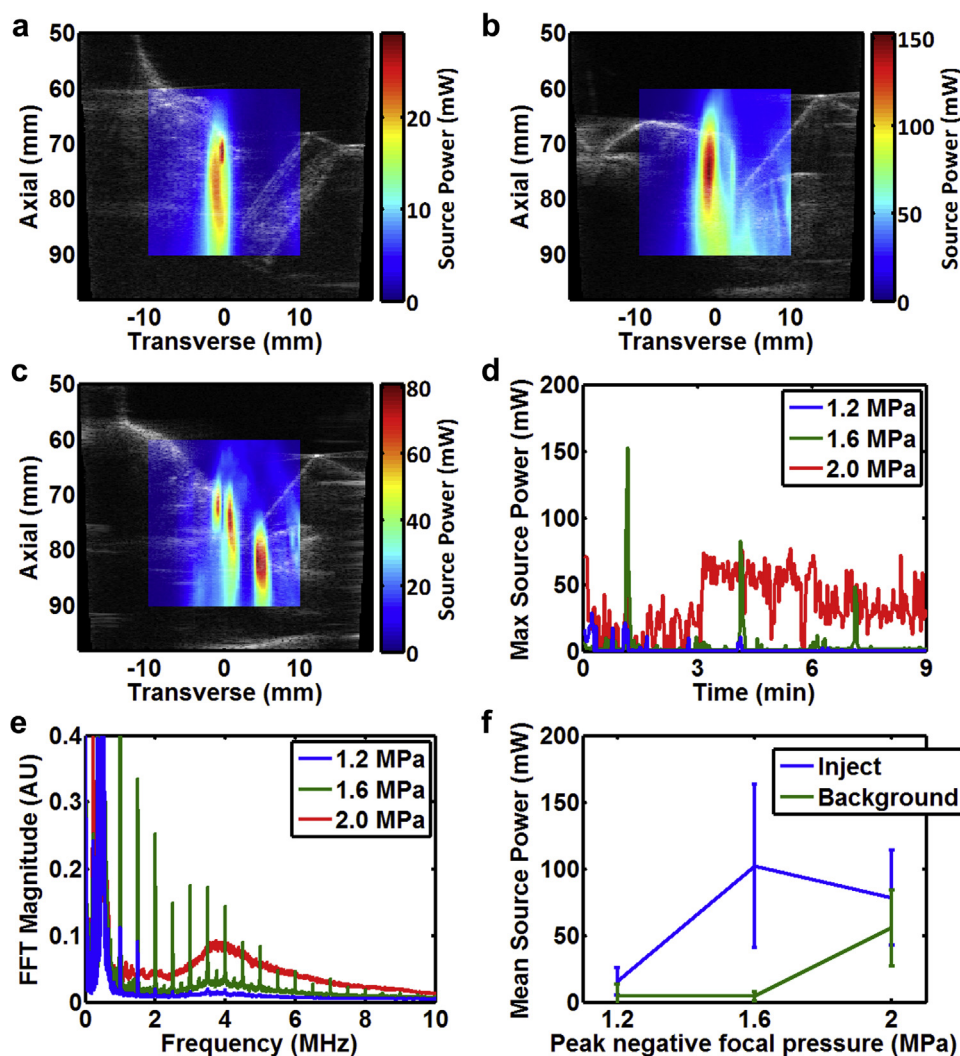


Fig. 5. B-mode and passive acoustic mapping (PAM) results for *in vivo* pressure ramp. (a–c) B-Mode with PAM overlay indicating peak source power for 1.2-, 1.6- and 2.0-MPa peak negative focal pressures. The mouse body (left), tumour (centre) and non-magnetic bar (right) are visible in the B-mode image. The rightmost area overlapping with the metal bar in (c) is an artefact caused by reflection against the metal surface which was significant only at this amplitude. (d) Maximum source power and (e) spectra for the three pressures. (f) Mean and standard deviation of source power at the three injection points (1, 4 and 7 min) versus background cavitation 1 min before each injection (0, 3 and 6 min). FFT = fast Fourier transform.

1994) with multiple harmonic peaks visible up to several megahertz, smaller ultraharmonic peaks (associated with stable cavitation) and an increase in the broadband signal level (associated with inertial cavitation).

Finally, at 2.0 MPa peak negative focal pressure (Fig. 5c), multiple regions of cavitation were observed close to the ultrasound focus, with lower peak amplitude (peak power 81.1 mW) than at 1.6 MPa. The evolution of this behaviour over time (Fig. 5d, red line) illustrates that cavitation occurred immediately, even before microbubbles were injected, while the spectrum (Fig. 5e, red line) was dominated by broadband noise.

The results for the three pressure steps may be summarised by extracting the cavitation power after each injection (1, 4 and 7 min) and comparing this with the background cavitation 1 min before each injection (0, 3 and 6 min). This is illustrated in Figure 5f. A large increase in the mean source power on injection was observed at 1.6 and 2.0 MPa compared with 1.2 MPa; however, this was only significantly above the background response at 1.6 MPa. These results suggest that increasing the pressure from 1.2 to 1.6 MPa resulted in a higher-amplitude response, probably because of the greater treated area (and hence number of microbubbles) being above the threshold for cavitation. At 2.0 MPa, cavitation was initiated even without microbubble injection, implying that the inertial cavitation threshold for tissue was exceeded. This result is commensurate with previous work in the literature at this frequency (Hynynen 1991). A pressure of 2.0 MPa was therefore unsuitable for these experiments as the acoustic emissions were no longer correlated with microbubble injection. To maximise the signal to noise (and avoid endogenous cavitation), a 1.6-MPa peak negative focal pressure was selected for use in subsequent experiments. This is similar to that employed in previous studies at this frequency using SonoVue (Choi *et al.* 2014; Coviello *et al.* 2015).

Effect of magnetic targeting on cavitation behaviour in vivo

The effect of magnetic targeting on the cavitation behaviour of MMBs *in vivo* is summarised in Figure 6, which contains B-mode images with PAM maps for the pulse containing the highest power response displayed as an overlay. Under the influence of the magnet, the maximum source power increased by 29% from 167.9 mW without a magnet to 216.0 mW with a magnet (Fig. 6a, b), reaching a level similar to that obtained with SonoVue (227.8 mW) (Fig. 6c). With use of a sample of MMBs with depleted bubble concentration, the maximum source power was an order of magnitude lower (16.5 mW), as expected.

Over the six injections per condition (Fig. 6e), magnetic targeting significantly increased the level of cavitation power detected within the tumour obtained using MMB, by >50% (mean: 122.6 mW without a magnet, 186.3 mW with a magnet, $p < 0.01$). The mean cavitation power observed using the commercial contrast agent SonoVue (232.5 mW) was not significantly higher than that with MMBs with magnetic targeting ($p > 0.05$). The response from the depleted MMB sample remained low (mean source power: 10.1 mW).

These results suggest that magnetic targeting was able to increase the local microbubble concentration *in vivo*, resulting in approximately 50% higher maximum cavitation power as observed using PAM. The magnitude of the effect of targeting was lower than that observed in previous *in vitro* studies (*ca.* 2×) (Crake *et al.* 2015), which is unsurprising because of the numerous unknown or adverse factors (flow rate; vascularity; vessel size, depth and location, *etc.*) that cannot be readily controlled *in vivo*.

The commercial contrast agent SonoVue did result in a slightly higher peak cavitation power than MMBs, even with magnetic targeting. This is most likely due to factors such as unequal microbubble concentration that could not be controlled within these *in vivo* experiments (at the high end, the quoted concentration of 5×10^8 microbubbles/mL for SonoVue [Schneider 1999] is more than 2.5 times that measured for MMBs). Other differences in formulation such as the components of MMBs that give them additional functionality over SonoVue (*i.e.*, iron oxide for targeting and MRI visibility, and fluorescent dye for tracking and as a model payload) could also have an effect on microbubble response and thus reduce the cavitation response of MMBs compared with simpler agents that lack such features. Nonetheless, the 50% increase in cavitation power observed using MMBs with magnetic targeting suggests a significant increase in local microbubble concentration was achieved, which could be important for cavitation-enhanced therapies. If the microbubbles were engineered also to deliver a drug, then the biological effect of targeting could be magnified as a result of increasing both the power of cavitation (resulting in extravasation of the drug) and its local concentration as a result of targeting. This hypothesis is tested in the next section by examining the quantity of fluorescent dye recovered from tumours after each experiment.

Effect of magnetic targeting on dose found in tumour

The effect of magnetic targeting on the quantity of fluorescent dye recovered from tumours after treatment is summarised in Figure 7. The result for SonoVue (corresponding to an implied dose of $0.13 \pm 0.01\%$) represents the background signal caused by such effects as

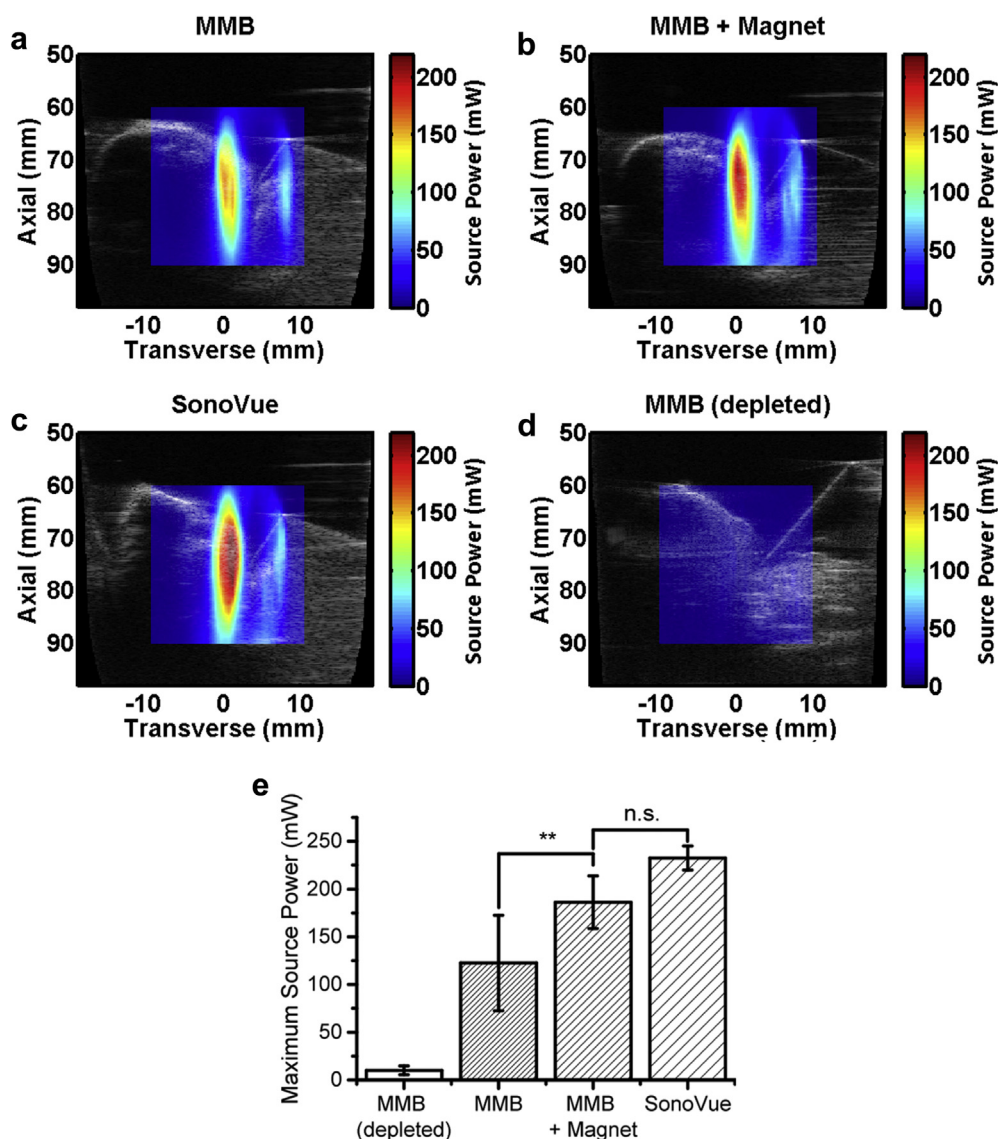


Fig. 6. Effect of magnetic targeting on cavitation behaviour *in vivo*. (a–d) B-Mode images with passive acoustic mapping (PAM) overlay for the pulse with highest power for (a) magnetic microbubbles (MMBs), (b) MMBs + magnet, (c) SonoVue and (d) depleted (24-h-old) MMBs. (e) Maximum source power for six injections per condition for the depleted (24-h-old) MMBs sample, MMBs, MMBs + magnet and SonoVue. Mean value is shown over six repeats per condition; error bars represent standard deviation. Asterisks represent statistical significance assessed using one-way analysis of variance followed by Tukey multiple comparison test (n.s. = not significant; $**p < 0.01$; comparisons not shown have p values < 0.001).

variability in tissue autofluorescence; all of the measurements taken using MMBs were significantly ($p < 0.01$) greater than this background reading. When the depleted MMB sample was used, the dose found in the tumour ($0.30 \pm 0.04\%$) was within the range of the mice in the distribution study discussed above. When MMBs were used without a magnet, the dose in the tumour more than doubled, compared with that for the depleted MMB sample, to $0.63 \pm 0.02\%$. The addition of a magnet was accompanied by a significant ($p < 0.01$) further rise in fluorescence to a dose of $0.75 \pm 0.03\%$.

Magnetic resonance imaging

In Figure 8 are magnetic resonance images from MMB-treated and saline control mice. Slices revealing the liver and tumour in each of the mice were selected, and the borders of these regions outlined manually. Under T2*-weighted imaging, iron oxide content appears as negative contrast (Chavhan et al. 2009; Na et al. 2009). This is clearly seen in the liver of the treatment mouse (Fig. 8a), which appears far darker than that of the control mouse (Fig. 8b) at a given echo time. This negative contrast results in a lower mean image intensity within

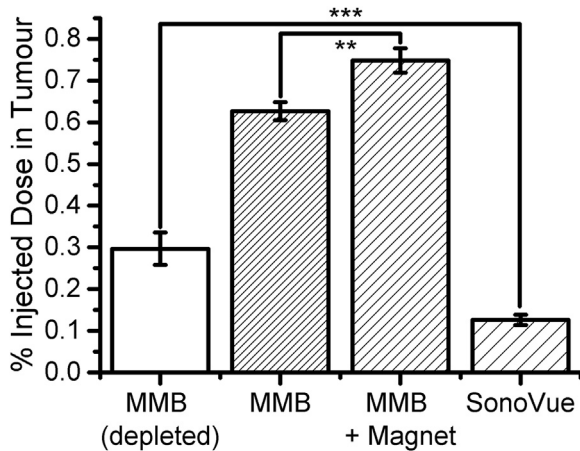


Fig. 7. Effect of magnetic targeting on dose recovered from tumour *in vivo*. Mean dose calculated from fluorescence measurements is shown from three tumour samples for each condition (magnetic microbubbles [MMBs], depleted [24-h-old] MMBs, MMBs + magnet and SonoVue). Error bars represent standard deviations. Asterisks represent statistical significance assessed using one-way analysis of variance followed by Tukey multiple comparison test (** $p < 0.01$, *** $p < 0.001$, comparisons not shown have p values < 0.0001).

the liver and more pronounced decay with increasing echo time compared with the control mouse (Fig. 8c), suggesting that a substantial proportion of the magnetic material from the bubbles is captured by the liver. The standard deviation of the image intensity within the liver (Fig. 8c, error bars) also declines with echo time (in contrast to the control mouse, in which it increases slightly), suggesting that the magnetic material was homogeneously distributed throughout the organ (therefore masking the normally inhomogeneous appearance of the liver seen in the control mouse). These results are in agreement with previous work with PVA-based microbubbles containing iron oxide that indicated negative contrast in the liver under T2*-weighted imaging as early as 10 min from injection (Barrefelt *et al.* 2013). As outlined above, in accordance with this result, substantial fluorescence from the DiI-stained lipid was also observed in the liver.

Dark areas of negative contrast were visible over the central portion of the tumour in the treatment mouse (Fig. 8d), whereas the control mouse tumour appeared largely homogenous (Fig. 8e). With increasing echo time, the mean intensity in the tumour of the treatment mouse declined compared with that of the control mouse (in which the mean intensity was approximately flat or slightly rising) (Fig. 8f). The standard deviation of image intensity in the treatment mouse (Fig. 8f, error bars) was greater than that in the control mouse and increased with echo time because of the inhomogeneous distribution of magnetic particles. This implies that a detectable quantity

of magnetic material from the microbubbles was retained in the tumour. It should be noted that the ultrasound duty cycle used in these experiments was very low (0.01%), and the magnet was not applied to the tumour for 5 min between the end of experiments and mouse euthanasia. The inhomogeneous distribution of particles in the tumour and clustering around the centre are also notable, as these coincide with the region exposed to both ultrasound and the magnetic field.

Summary and limitations

The results presented here suggest that magnetic targeting was able to increase the magnitude of microbubble-induced cavitation, and this resulted in deposition of a greater quantity of microbubble components in the tumour. Previous studies have attributed such effects to extravasation (Bazan-Peregrino *et al.* 2013) and/or microscopic vessel damage (Hwang *et al.* 2006) as a result of inertial cavitation: The spectra of cavitation emissions observed in these *in vivo* experiments were broadband in nature, suggesting this could be the dominant mechanism here. MMBs resulted in cavitation with maximum amplitude similar to that of SonoVue, and were associated with a significant (twofold) increase in the MMB dose calculated from fluorescence measurements compared with depleted samples with lower acoustic response. The addition of a magnet resulted in a modest increase in the peak cavitation power, suggesting that magnetic targeting was able to transiently increase the local microbubble concentration, resulting in higher instantaneous cavitation power.

Although the results presented here are promising and magnetic targeting was found to significantly increase both cavitation power and deposition of material in the tumours, in absolute terms the percentage of injected dose recovered (and incremental change in this with targeting) remained small. There are several potential reasons for this which could be optimised in future studies to improve the efficacy of the magnetic targeting protocol and subsequent delivery:

First, the ultrasound conditions used were particularly mild in this study (100 cycles per burst at 0.5-Hz PRF, duty cycle 0.01%) compared with duty cycles of 6–90% employed in previous studies that aimed to explicitly promote extravasation (Bazan-Peregrino *et al.* 2012). As the primary aim of this study was not extravasation, but rather establishment of whether a new MMB formulation could promote cavitation *in vivo* (no therapeutic agent was used at this stage), this shorter burst length was intended to reduce microbubble destruction by ultrasound and therefore improve circulation time. However, the rapid decline in cavitation response after injection observed *in vivo* (Fig. 5d) and the relatively similar

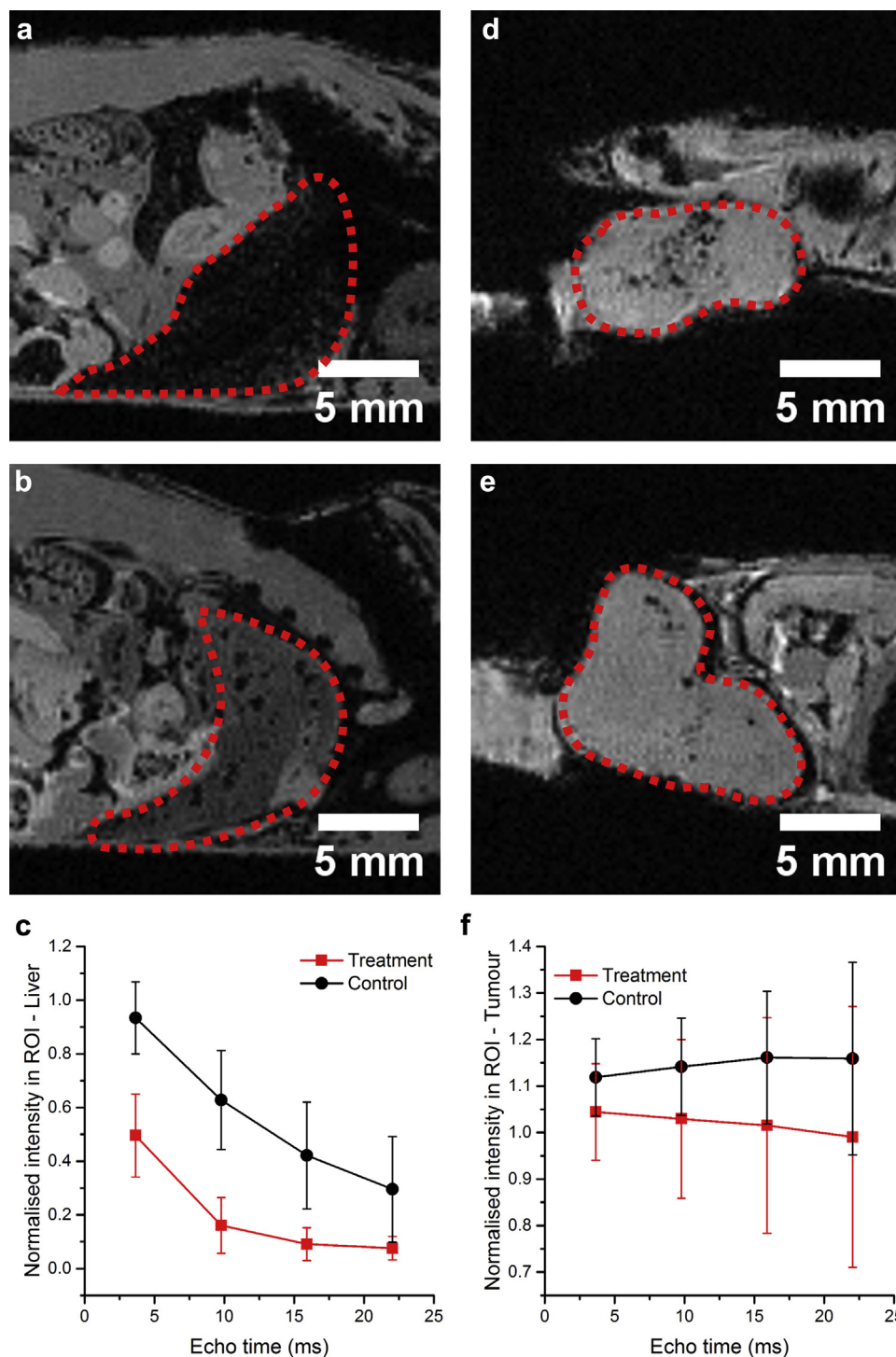


Fig. 8. (a–c) Magnetic resonance imaging and analysis for liver of (a) treated mouse and (b) control mouse (echo time = 9.78 ms) (c) Normalised intensity and standard deviation in liver region of interest (ROI) for treatment mouse and control mouse versus echo time. (d–f) Magnetic resonance images and analysis for tumour of (d) treated mouse and (e) control mouse (echo time = 15.91 ms). (f) Normalised intensity and standard deviation in tumour ROI for treatment mouse and control mouse versus echo time. ROIs are represented by red outlines in the images.

response of SonoVue in the same setup using 50,000 cycle pulses (vs. 100 cycles here) (Graham 2014) suggest that biological clearance mechanisms are by far the domi-

nant factor. These findings should be considered in the design of future studies to maximise the impact of the microbubbles during their circulation time, for instance, by

increasing the burst length and/or PRF over a shorter total treatment time.

Second, the magnet used for targeting was in this case a single permanent magnet of high strength and approximately the same size as the tumours. The magnet was manually positioned close to the tumours, where its position was further constrained by the requirement to avoid excessive interference with the ultrasound field. Such an arrangement is likely not optimal and could result in a combination of both “undertargeting” (in which the field strength in the tumour was too low to optimally retain bubbles) or “overtargeting” (in which bubbles were pulled toward the magnet beyond the intended site, such as into the skin or elsewhere in the mouse). The solution to this issue is clearly a non-trivial problem, but could involve more complicated arrangements of permanent magnets (Barnsley *et al.* 2015) or electromagnets (Mathieu and Martel, 2010) designed to achieve higher field gradients and, thus, greater targeting efficacy.

Finally, the small needle gauge used to deliver microbubbles (29 gauge) may also have reduced the effective microbubble concentration reaching the tumour. Larger-diameter needles have been reported to preserve more bubbles (Browning *et al.* 2011), but this may come at the expense of more difficult cannula placement for tail vein injection. Other factors such as the rate of injection may also affect the microbubbles and could be tested in future studies.

Nonetheless, even subject to the modest ultrasound conditions and simple magnet used here, a significant increase in both acoustic emissions and fluorescence suggests that ultrasound-induced cavitation of MMBs did result in extravasation of fluorescent material from the bubbles and that this could be at least moderately improved using magnetic targeting. The discrete hypointense regions observed under MRI suggest the same is true of the microbubbles’ iron content, and confirm that further study of nanoparticle delivery from microbubbles with MRI is worthwhile. Optimisation of the ultrasound and magnetic targeting setup, addition of therapeutic drugs and investigation of the effects on distribution and treatment efficacy will be the subject of future studies.

CONCLUSIONS

In this study, the *in vivo* distribution and ability to promote cavitation of fluorescently labelled magnetic microbubbles were investigated in a murine tumour model. It was found that fluorescence from the microbubbles could be detected in blood and organs from treated mice, while their iron content was visible as negative contrast on MRI. Cavitation was observed using passive

acoustic mapping under focused ultrasound excitation and found to be comparable to that produced by a commercial contrast agent, with the additional benefits of facilitating MRI contrast and ability to carry a payload (here illustrated using a fluorescent dye). Cavitation induced by the microbubbles and magnetic targeting were both found to be associated with increased fluorescence in excised tumours. This provides evidence both for the magnetic microbubbles as a means of facilitating delivery *in vivo* and for PAM as a means of non-invasively monitoring this process.

Acknowledgments—The authors thank Apurva Shah for assistance during animal experiments, Richard Browning for assistance with microbubble manufacture and James Fisk and David Salisbury for construction of the transducer and phantom holders used in this study. Calum Crane acknowledges the support of RCUK Digital Economy Programme Grant EP/G036861/1 (Oxford Centre for Doctoral Training in Healthcare Innovation). In addition the authors are grateful to the EPSRC for supporting this research through Grant EP/I021795/1 and Programme Grant EP/L024012/1 (OxCD3: Oxford Centre for Drug Delivery Devices).

REFERENCES

- Barnsley LC, Carugo D, Owen J, Stride E. Halbach arrays consisting of cubic elements optimised for high field gradients in magnetic drug targeting applications. *Phys Med Biol* 2015;60:8303.
- Barrefelt Å, Saghaian M, Kuiper R, Ye F, Egri G, Klickermann M, Brismar TB, Aspelin P, Muhammed M, Dähne L, Hassan M. Biodistribution, kinetics, and biological fate of SPION microbubbles in the rat. *Int J Nanomedicine* 2013;8:3241–3254.
- Bazan-Peregrino M, Arvanitis CD, Rifai B, Seymour LW, Coussios CC. Ultrasound-induced cavitation enhances the delivery and therapeutic efficacy of an oncolytic virus in an *in vitro* model. *J Control Release* 2012;157:235–242.
- Bazan-Peregrino M, Rifai B, Carlisle RC, Choi J, Arvanitis CD, Seymour LW, Coussios CC. Cavitation-enhanced delivery of a replicating oncolytic adenovirus to tumors using focused ultrasound. *J Control Release* 2013;169:40–47.
- Browning RJ, Mulvana H, Tang M, Hajnal JV, Wells DJ, Eckersley RJ. Influence of needle gauge on *in vivo* ultrasound and microbubble-mediated gene transfection. *Ultrasound Med Biol* 2011;37:1531–1537.
- Butler B, Hills B. The lung as a filter for microbubbles. *J Appl Physiol* 1979;47:537–543.
- Carlisle R, Choi J, Bazan-Peregrino M, Laga R, Subr V, Kostka L, Ulbrich K, Coussios CC, Seymour LW. Enhanced tumor uptake and penetration of virotherapy using polymer stealthing and focused ultrasound. *J Natl Cancer Inst* 2013;105:1701–1710.
- Chavhan GB, Babyn PS, Thomas B, Shroff MM, Haacke EM. Principles, techniques, and applications of T2*-based MR imaging and its special applications. *Radiographics* 2009;29:1433–1449.
- Cheng X, Li H, Chen Y, Luo B, Liu X, Liu W, Xu H, Yang X. Ultrasound-triggered phase transition sensitive magnetic fluorescent nanodroplets as a multimodal imaging contrast agent in rat and mouse model. *PLoS One* 2013;8:e85003.
- Choi JJ, Carlisle RC, Coviello C, Seymour L, Coussios CC. Non-invasive and real-time passive acoustic mapping of ultrasound-mediated drug delivery. *Phys Med Biol* 2014;59:4861–4877.
- Coussios CC, Roy RA. Applications of acoustics and cavitation to noninvasive therapy and drug delivery. *Annu Rev Fluid Mech* 2008;40:395–420.
- Coviello C, Kozick R, Choi J, Gyöngy M, Jensen C, Smith PP, Coussios CC. Passive acoustic mapping utilizing optimal beamforming in ultrasound therapy monitoring. *J Acoust Soc Am* 2015;137:2573–2585.

- Crake C, de Saint Victor M, Owen J, Coviello C, Collin J, Coussios CC, Stride E. Passive acoustic mapping of magnetic microbubbles for cavitation enhancement and localization. *Phys Med Biol* 2015;60:785–806.
- Dayton P, Klivanov A, Brandenburger G, Ferrara K. Acoustic radiation force in vivo: A mechanism to assist targeting of microbubbles. *Ultrasound Med Biol* 1999;25:1195–1201.
- Diehl KH, Hull R, Morton D, Pfister R, Rabemampianina Y, Smith D, Vidal JM, Vorstenbosch CVD. A good practice guide to the administration of substances and removal of blood, including routes and volumes. *J Appl Toxicol* 2001;21:15–23.
- Ferrara K, Pollard R, Borden M. Ultrasound microbubble contrast agents: Fundamentals and application to gene and drug delivery. *Annu Rev Biomed Eng* 2007;9:415–447.
- Graham SM. Ultrasound-triggered drug release from liposomes using nanoscale cavitation nuclei. DPhil thesis, University of Oxford, 2014.
- Greenleaf WJ, Bolander ME, Sarkar G, Goldring MB, Greenleaf JF. Artificial cavitation nuclei significantly enhance acoustically induced cell transfection. *Ultrasound Med Biol* 1998;24:587–595.
- Gyöngy M, Coussios CC. Passive spatial mapping of inertial cavitation during HIFU exposure. *IEEE Trans Biomed Eng* 2010;57:48–56.
- Ham AS, Klivanov AL, Lawrence MB. Action at a distance: Lengthening adhesion bonds with poly(ethylene glycol) spacers enhances mechanically stressed affinity for improved vascular targeting of microparticles. *Langmuir* 2009;25:10038–10044.
- Hua J, Erickson LE, Yiin TY, Glasgow LA. A review of the effects of shear and interfacial phenomena on cell viability. *Crit Rev Biotechnol* 1993;13:305–328.
- Hwang JH, Tu J, Brayman AA, Matula TJ, Crum LA. Correlation between inertial cavitation dose and endothelial cell damage in vivo. *Ultrasound Med Biol* 2006;32:1611–1619.
- Hynynen K. The threshold for thermally significant cavitation in dog's thigh muscle in vivo. *Ultrasound Med Biol* 1991;17:157–169.
- Hynynen K, McDannold N, Vykhotseva N, Raymond S, Weissleder R, Jolesz FA, Sheikov N. Focal disruption of the blood–brain barrier due to 260-kHz ultrasound bursts: A method for molecular imaging and targeted drug delivery. *J Neurosurg* 2006;105:445–454.
- Illing RO, Kennedy JE, Wu F, ter Haar GR, Protheroe AS, Friend PJ, Gleeson FV, Cranston DW, Phillips RR, Middleton MR. The safety and feasibility of extracorporeal high-intensity focused ultrasound (HIFU) for the treatment of liver and kidney tumours in a Western population. *Br J Cancer* 2005;93:890–895.
- Kremkau WK. Cancer therapy with ultrasound: A historical review. *J Clin Ultrasound* 1979;7:287–300.
- Lafon C, Somaglino L, Bouchoux G, Mari JM, Chesnais S, Ngo J, Mestas JL, Fossheim SL, Nilssen EA, Chapelon JY. Feasibility study of cavitation-induced liposomal doxorubicin release in an AT2 Dunning rat tumor model. *J Drug Targeting* 2012;20:691–702.
- Leighton TG. The acoustic bubble. London: Academic Press; 1994.
- Lentacker I, De Smedt SC, Sanders NN. Drug loaded microbubble design for ultrasound triggered delivery. *Soft Matter* 2009;5:2161–2170.
- Liu Z, Lammers T, Ehling J, Fokong S, Bornemann J, Kiessling F, Gätjens J. Iron oxide nanoparticle-containing microbubble composites as contrast agents for MR and ultrasound dual-modality imaging. *Biomaterials* 2011;32:6155–6163.
- Lum AFH, Borden MA, Dayton PA, Kruse DE, Simon SI, Ferrara KW. Ultrasound radiation force enables targeted deposition of model drug carriers loaded on microbubbles. *J Control Release* 2006;111:128–134.
- Mannell H, Pircher J, Räthel T, Schilberg K, Zimmermann K, Pfeifer A, Mykhaylyk O, Gleich B, Pohl U, Krötz F. Targeted endothelial gene delivery by ultrasonic destruction of magnetic microbubbles carrying lentiviral vectors. *Pharm Res* 2012;29:1282–1294.
- Mathieu JB, Martel S. Steering of aggregating magnetic microparticles using propulsion gradients coils in an MRI scanner. *Magn Reson Med* 2010;63:1336–1345.
- Miller DL, Thomas RM. Ultrasound contrast agents nucleate inertial cavitation in vitro. *Ultrasound Med Biol* 1995;21:1059–1065.
- Mulvana H, Eckersley RJ, Browning R, Hajnal JV, Stride E, Barrack T, Tang M, Pankhurst Q, Wells D. Enhanced gene transfection in vivo using magnetic localisation of ultrasound contrast agents: preliminary results. In 2010 IEEE International Ultrasonics Symposium 2010. IEEE, 670–673.
- Na HB, Song IC, Hyeon T. Inorganic nanoparticles for MRI contrast agents. *Adv Mater* 2009;21:2133–2148.
- Newman CM, Lawrie A, Briskin AF, Cumberland DC. Ultrasound gene therapy: On the road from concept to reality. *Echocardiography* 2001;18:339–347.
- Patil AV, Rychak JJ, Klivanov AL, Hossack JA. A real-time technique for improving molecular imaging and guiding drug delivery in large blood vessels: In vitro and ex vivo results. *Mol Imaging* 2011;10:238.
- Patrick MK. Ultrasound in physiotherapy. *Ultrasonics* 1966;4:10–14.
- Plank C, Vlaskou D, Schillinger U, Mykhaylyk O, Brill T, Rudolph C, Huth S, Krötz F, Hirschberger J, Bergemann C. Localized nucleic acid delivery using magnetic nanoparticles. *Eur Cell Mater* 2005;10:8.
- Roberts WW, Hall TL, Ives K, Wolf JS Jr, Fowlkes JB, Cain CA. Pulsed cavitation ultrasound: A noninvasive technology for controlled tissue ablation (histotripsy) in the rabbit kidney. *J Urol* 2006;175:734–738.
- Schneider M. Characteristics of SonoVue™. *Echocardiography* 1999;16:743–746.
- Sennoga CA, Mahue V, Loughran J, Casey J, Seddon JM, Tang M, Eckersley RJ. On sizing and counting of microbubbles using optical microscopy. *Ultrasound Med Biol* 2010;36:2093–2096.
- Stride E, Porter C, Prieto AG, Pankhurst Q. Enhancement of microbubble mediated gene delivery by simultaneous exposure to ultrasonic and magnetic fields. *Ultrasound Med Biol* 2009;35:861–868.
- Takalkar AM, Klivanov AL, Rychak JJ, Lindner JR, Ley K. Binding and detachment dynamics of microbubbles targeted to P-selectin under controlled shear flow. *J Control Release* 2004;96:473–482.
- ter Haar G. Therapeutic ultrasound. *Eur J Ultrasound* 1999;9:3–9.
- Unger EC, McCreery TP, Sweitzer RH, Caldwell VE, Wu Y. Acoustically active lipospheres containing paclitaxel: A new therapeutic ultrasound contrast agent. *Invest Radiol* 1998;33:886–892.
- Villanueva FS, Jankowski RJ, Klivanov S, Pina ML, Alber SM, Watkins SC, Brandenburger GH, Wagner WR. Microbubbles targeted to intercellular adhesion molecule-1 bind to activated coronary artery endothelial cells. *Circulation* 1998;98:1–5.
- Vlaskou D, Mykhaylyk O, Krötz F, Hellwig N, Renner R, Schillinger U, Gleich B, Heidsieck A, Schmitz G, Hensel K, Plank C. Magnetic and acoustically active lipospheres for magnetically targeted nucleic acid delivery. *Adv Funct Mater* 2010a;20:3881–3894.
- Vlaskou D, Pradhan P, Bergemann C, Klivanov AL, Hensel K, Schmitz G, Plank C, Mykhaylyk O. Magnetic microbubbles: Magnetically targeted and ultrasound-triggered vectors for gene delivery in vitro. *AIP Conf Proc* 2010b;1311:485–494.
- Vovk U, Pernus F, Likar B. A review of methods for correction of intensity inhomogeneity in MRI. *IEEE Trans Med Imaging* 2007;26:405–421.
- Yang F, Li Y, Chen Z, Zhang Y, Wu J, Gu N. Superparamagnetic iron oxide nanoparticle-embedded encapsulated microbubbles as dual contrast agents of magnetic resonance and ultrasound imaging. *Biomaterials* 2009;30:3882–3890.